Understanding the pressure effect on the elastic, electronic, vibrational, and bonding properties of $CeScO_3$ perovskite

Tarik Ouahrani,[*,†,‡] Fatima-Zohra Medjdoub,[¶] Saber Gueddida,[§] Álvaro Lobato Fernandez,[‖] Ruth Franco,[‖] Nour-Eddine Benkhettou,[¶] Michael Badawi,[§] Akun Liang,[⊥] Jesus Gonzalez,[#] and Daniel Errandonea[*,⊥]

†*Laboratoire de Physique Théorique, Université de Tlemcen, Algeria.*

‡*École supérieures en sciences appliquées, B.P. 230, 13000 Tlemcen Algeria.*

¶*Laboratoire des Matériaux Magnétiques, Faculté des Sciences, Université Djillali Liabes de Sidi Bel-Abbès, Sidi Bel-Abbés 22000, Algeria*

§*Université de Lorraine, LPCT, UMR 7019, 54506 Vandoeuvre-lès-Nancy, France*

‖*MALTA-Consolider Team and Departamento de Química Física y Analítica, Universidad de Oviedo, E-33006 Oviedo, Spain*

⊥*Departamento de Física Aplicada - Instituto de Ciencia de Materiales, Matter at High Pressure (MALTA) Consolider Team, Universidad de Valencia, Edificio de Investigación, C/Dr. Moliner 50, Burjassot, 46100, Valencia, Spain*

#*Department of Earth Sciences and Condensed Matter Physics (CITIMAC), Universidad de Cantabria (UNICAN), Spain*

E-mail: tarik_ouahrani@yahoo.fr; daniel.errandonea@uv.es

Abstract

$CeScO_3$ is a promising perovskite-type material that presents the characteristic to remain highly stable upon compression, contrary to other perovskite compounds that often undergo phase transformations under pressure. In contrast with the structural behavior of $CeScO_3$, the influence of pressure on other of its physical properties, such as electronic, vibrational, atomic and polyhedral bulk and elastic properties, is still unknown. In this work, we propose to fill this gap by a combination of computational quantum-mechanics methodologies based on density-functional theory and high-pressure Raman spectroscopy experiments. In particular, the influence of pressure in the crystal structure has been studied, up to 40 GPa, and compared with previous experiments showing that density-functional theory properly describes the changes induced by pressure in $CeScO_3$. Calculations have also been used to obtain phonon frequencies and their pressure dependence, and to propose a mode-symmetry assignment. From Raman experiments we have obtained the frequency and pressure dependence of lattice vibrations involving changes in polarisability, validating phonon calculations, which give not only Raman-active but also infrared-active and silent modes. In addition, phonon-dispersion and elastic-constant calculations are consistent with the structural stability of an orthorhombic perovskite-type up to 40 GPa. Finally, we provide a description of the electronic band structure, showing that $CeScO_3$ has a much smaller band-gap than other scandates due to the role of Ce f-electrons. Such electrons also cause a closing of the electronic band-gap under compression.

INTRODUCTION

Magneto-resistance,[1] ferroelectricity,[2] superconductivity,[3] and high electrocatalytic reactivity[4] are some of the most requested properties of materials for developing novel technological applications. A group of materials that have many of these properties is the family of perovskite-type oxides;[5,6] in particular rare-earth scandates with the chemical formula $REScO_3$ (RE= rare-earth element). These materials also bear many other interesting characteristics. To list some of them, we can mention the fact that they have high-dielectric constants and wide electronic band-gaps with values in cases larger than 6 eV.[7] Particularly, orthorhombic $CeScO_3$ is a promising compound that can be manufactured by means of low-cost and non-contaminant procedures.[8,9] As part of the characterization of $CeScO_3$, required for its use in applications, this material was subjected to ambient pressure studies.[8,9] On top of that, there is a recent investigation[10] where it was analyzed under the application of hydrostatic and non-hydrostatic pressure. According to this study, $CeScO_3$ is highly stable under compression, which contrasts with the behavior of other perovskites. In special, structural phase transition do not take place up to 40 GPa, which is important for applications designed to work under high stresses.[11] However, little more is known on the influence of pressure on the physical properties of $CeScO_3$, in particular, the electronic, vibrational, and elastic properties.

The high-pressure (HP) behavior of $CeScO_3$ is also interesting for fundamental research.[10] According to the above-described results on structural stability, the HP behavior of $CeScO_3$ is very different from that of many other RE perovskites which experience phase transitions at relatively low pressure; in cases below 3 GPa. We can list among them, $LaGaO_3$ which undergoes a structural phase transition at 2.5 GPa,[12] as well as $GdMnO_3$,[13,14] and $LaAlO_3$[15] which exhibit a rich polymorphic sequence under the application of HP. It has been argued that the cause of the structural transformations driven by pressure is related to the modification under compression of the strict geometric rules satisfied by perovskites.[10] Therefore, it is important to study the effect of pressure not only in the unit-cell parameters of $CeScO_3$,

but also in polyhedral units, which can be distorted or tilted in order to accommodate external pressure. This has been successfully done in the past in related compounds utilizing density-functional theory (DFT) calculations.[16,17] Such computing simulations can also provide useful information on the elastic, vibrational, and electronic properties of $CeScO_3$ and their behavior under compression.

In this work, we report a systematic density-functional theory study of $CeScO_3$ under compression up to 40 GPa. We have studied the changes induced by pressure in the crystal structure, elastic constants, lattice vibrations, and electronic properties. Furthermore, we will also focus on the analysis of the polyhedral and atomic contributions to the unit cell volume and the bulk compressibility. Quantum theory of atoms in molecules (QTAIM)[18] is chosen as an appropriate numerical tool to carry out the topological partition of the electronic density into the local constituents of the title compound under pressure. In order to complement the lattice dynamic calculations, we have also performed the first-time HP Raman spectroscopy studies. The results will be discussed in comparison with previous studies.[10]

EXPERIMENTAL METHODS

HP Raman experiments were carried out under quasi-hydrostatic conditions up to 12.7 GPa. The $CeScO_3$ sample was prepared using a two-step combustion synthesis method, involving calcination at 600 °C for 1 h in air and a subsequent vacuum heating at 1100 °C for 25 hs.[10] This sample was previously used for x-ray diffraction measurements,[10] which confirmed the perovskite-type structure for our sample of $CeScO_3$. Raman measurements were performed using a triple monochromator Jobin-Yvon T64000 in the subtractive mode with a resolution of 0.8 cm^{-1} (1800 grooves/mm grating and 100 μm entrance slit). The set-up allows us to make measurements for wavenumber larger than 140 cm^{-1}. It was equipped with a liquid nitrogen-cooled CCD detector. The excitation source was 514.5 nm argon laser-focused down

with a 20x objective. The laser power on the sample was below 5mW. HP conditions were generated with a membrane-type diamond-anvil cell (DAC) using a 4:1 methanol-ethanol mixture[19,20] as the pressure-transmitting medium. This medium is quasi-hydrostatic up to 10.5 GPa,[19] but can be used safely at higher pressure (up to 12.7 GPa in this study) for studying materials with low compressibility, which is the case of $CeScO_3$.[10] The pressure was determined using the ruby-fluorescence technique[21] (1% maximum uncertainty).

COMPUTATIONAL METHODS

The calculations reported here have been carried out using the widely used plane-wave *Vienna Ab initio Simulation Package* (VASP).[22,23] To consider both valence and the semi-core states, we have chosen the projector-augmented wave scheme (PAW)[24] implemented in this code. We also resorted to the use of semi-local functional, Perdew-Burke-Ernzerhof revised for solids (GGA-PBEsol)[25] exchange potential within the spin-polarized approach. This set-up has been successfully used for the prediction of structural properties.[26] To counteract the problems associated with the density-functional theory (DFT) self-interaction error,[27] which can artificially delocalize the on-site Coulombic interactions of d- and f-electrons, a DFT+U methodology is employed.[28] The Hubbard correction (U = 4.57 eV) were respectively applied to both Ce-4f and Sc-3d states.[28] The Brillouin zone mesh was set to $6 \times 4 \times 6$ **k**-points. Structural optimizations were deemed to be converged where all the forces are below a threshold of F_{tol} = 1.00 mRy/atom. The elastic constants were calculated within the stress-strain methodology implemented in the ELASTIC python routines,[29] surfaced to the VASP code.

Due to the discrepancy of VASP code to properly describe the strongly correlated f and d-Ce states,[30] and efficiently calculate the band gap value under pressure, we used the WIEN2K[31] code to study the electronic properties of $CeScO_3$. For this purpose, the optimization of the lattice parameters was redone under strict conditions, namely, the parameter

$R_{min} \times G_{max}$ was taken equal to 8, and the Fourier expanded charge density was truncated at $G_{max} = 12$, using WIEN2K. The self-consistency calculations were considered to be converged when the total energy difference between succeeding iterations is less than 10^{-5} Ry per formula unit.

Table 1: Unit-cell parameters and equation of state parameters of $CeScO_3$ according to our calculations and experiments (Expt).

	a (Å)	b (Å)	c (Å)	(V_0)(Å^3)	B_0(GPa)	B_0'
This work (PBEsol+U)	5.839(3)	8.051(6)	5.646(8)	265.5(1)	163(3)	5.2(5)
Expt[10]	5.777(6)	8.045(9)	5.642(6)	262.5(3)	165(7)	6.3(5)
Expt[38]	5.787(3)	8.047(8)	5.626(4)	–	–	–

Lattice-dynamics calculations were performed within the density-functional perturbation theory (DFPT)[32,33] using the direct-force constant approach (or supercell method) to study the phonon dispersion curves including the vibrational modes at the Γ point of the Brillouin Zone. All these calculations were carried out in a single self-consistent cycle by means of the PHONOPY[34] open-source package interfaced to VASP. This task requires the calculation of the ground state charge density and its linear response to external excitations.[35] The phonon frequencies are computed in a $2 \times 2 \times 2$ super-cell. The phonon density of states (PDOS) was obtained by integration of the phonon frequencies with a high number of **k**-points ($4 \times 4 \times 4$ Monkhorst-Pack grid).

Bonding properties have been also studied. To extract atomic volumes and local compressibilities, we employed CRITIC2 code.[36] The key point of this approach is the partition of the 3D real space of the unit cell into disjoint atomic basins (Ω), and then quantify the volume of each basin[37] by integration. Such an atomic-level calculation is based on the quantum theory of atoms in molecules (QTAIM)[18] theory. An equivalent polyhedral partition has been also carried out.

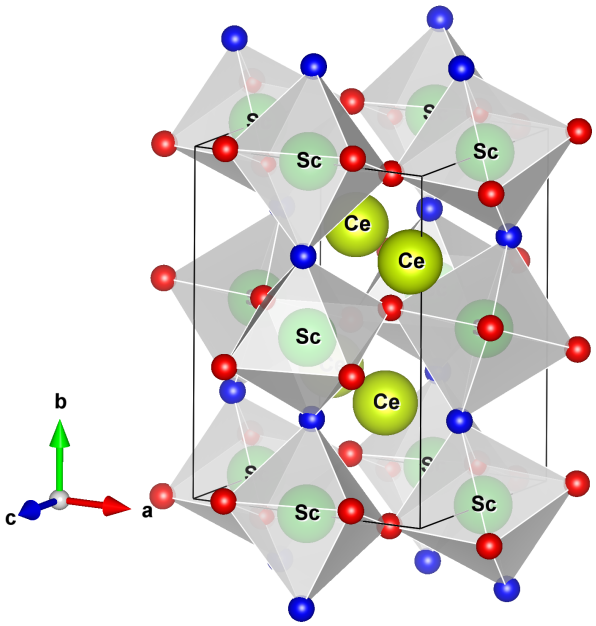

Figure 1: Crystal structure of $CeScO_3$. Scandium atoms are represented in light green, cerium atoms in yellow, and oxygen atoms in red (O_1) and blue (O_2). ScO_6 octahedral units are shown. CeO_{12} units are not shown for the sake of simplicity.

RESULTS AND DISCUSSIONS

EQUILIBRIUM GROUND STATE AND STRUCTURAL STABILITY

The crystal structure of $CeScO_3$ is shown in Fig. 1. The space group *Pnma* describes the orthorhombic structure. Sc atoms are in octahedral coordination and Ce^{3+} ions occupy the empty spaces formed by the corner-sharing framework made by ScO_6 octahedra. Ce atoms are coordinated by 8 nearest oxygen neighbors forming CeO_8 dodecahedra. Besides, there are four-second neighbor oxygens, based on that the coordination of Ce has been described in the literature as 8 + 4 leading to CeO_{12} cubo-octahedra.[8] Interestingly, ScO_6 and CeO_{12} fill out the whole unit cell volume since they share all the triangular faces, whereas the rhombic faces are shared between the cubo-octahedra (see below).

In order to optimize the crystal structure in DFT calculations; we have used a set of volumes that correspond to pressures ranging from -10 GPa to 40 GPa. At each volume, we

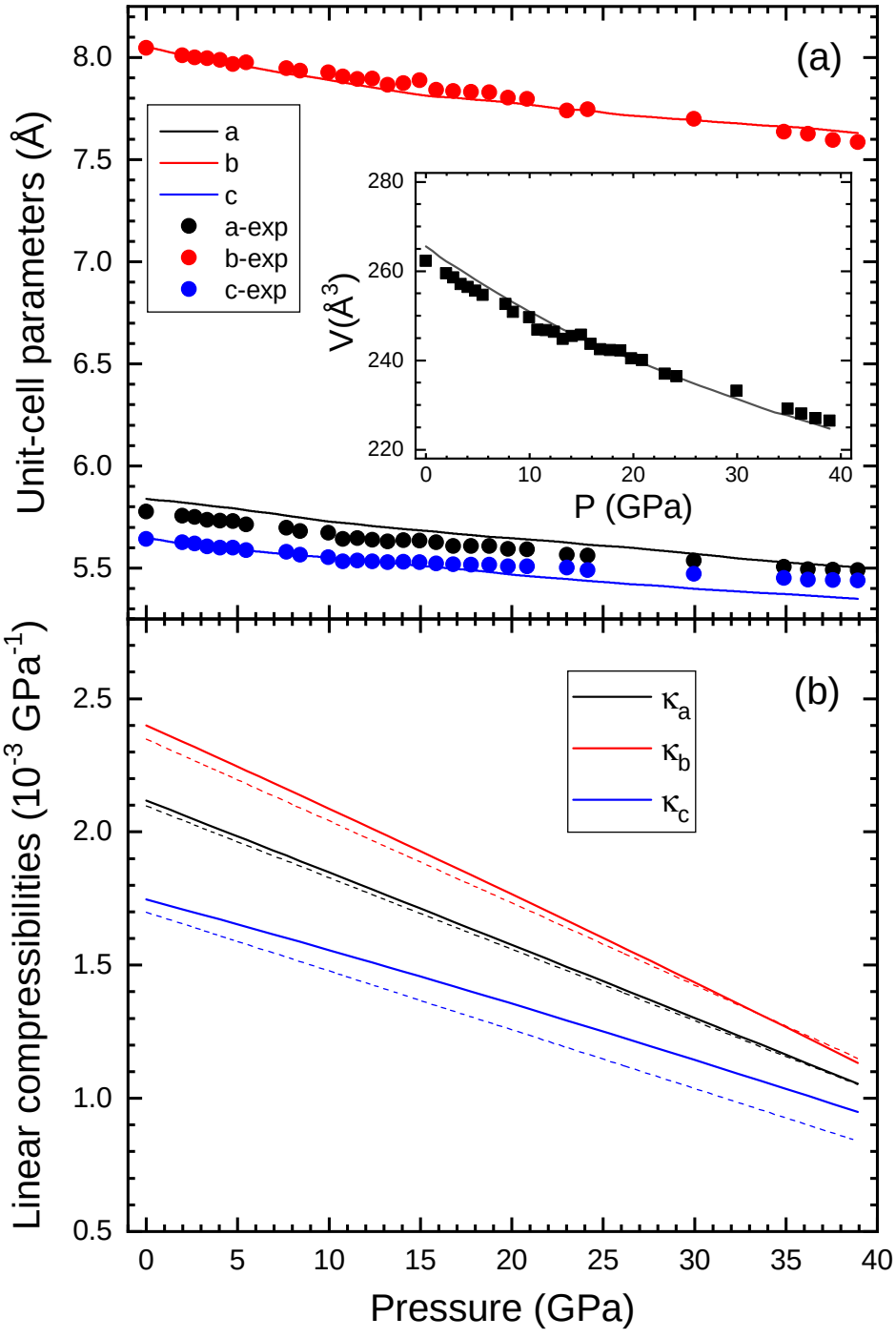

Figure 2: Pressure dependence of (a) calculated unit-cell parameters (lines) compared to experiments (symbols) from Ref. 10; (b) linear compressibility of different axes, results from this work are shown as solid lines and results obtained from Ref. 10 are shown with dotted lines. The inset shows the pressure dependence of the volume; lines are present calculations and symbols are experiments from Ref. 10.

have optimized the a, b, and c parameters as well as the atomic positions. The optimized crystal structure at ambient pressure compares very well with the experimental results as can be seen in Tables 1 and 2. This validates our PBEsol+U scheme to describe the crystal structure of $CeScO_3$. The evolution of the optimized unit-cell parameters as a function of pressure (P) is represented in Figure 2(a). We would like to remark that the change of lattice parameters upon compression is in good agreement with that measured by XRD.[10] This means that the non-hydrostatic conditions of the previous XRD experiments[10] do not have an important effect on the compressibility of $CeScO_3$. A similar good agreement is obtained for the pressure dependence of the volume as can be seen in the inset of Fig 2(a). Fig.2(b) represents the pressure dependence of linear compressibilities. The b parameter is the most affected by the application of pressure, whereas the c is the one that changes less under compression. This fact is a consequence of the distortion of ScO_6 octahedra. As pressure increases, linear compressibilities become similar, see Fig. 2(b). In fact, near 40 GPa the compressibility becomes rather isotropic.

Table 2: Optimized crystallographic coordinates of atoms in the $CeScO_3$ compound compared with available experimental ones of Ref. 10

Atom	Wyckoff position	x	y	z
Ce	4c	0.0559, 0.0375*	0.2500, 0.2500*	0.9864, 0.9808*
Sc	4b	0.0000, 0.0000*	0.0000, 0.0000*	0.5000, 0.5000*
O_1	4c	0.9622, 0.9770*	0.2500, 0.2500*	0.3979, 0.3860*
O_2	8d	0.2999, 0.2979*	0.0527, 0.0530*	0.6987, 0.7058*

*Experimental data from Ref.[10]

The calculated linear compressibilities at ambient pressure ($\kappa_a = \frac{-1}{a}\frac{\partial a}{\partial p}$, $\kappa_b = \frac{-1}{b}\frac{\partial b}{\partial p}$ and $\kappa_c = \frac{-1}{c}\frac{\partial c}{\partial p}$) are in good agreement with those determined from experiments.[10] The calculated values of κ_a and κ_b at zero P, are, respectively, 2.15×10^{-3} GPa^{-1} and 2.40×10^{-3} GPa^{-1}; very close to the measured values of $\kappa_a = 2.10 \times 10^{-3}$ GPa^{-1} and $\kappa_a = 2.35 \times 10^{-3}$ GPa^{-1}. Our calculated values of κ_c is also in concordance with experiments. Errandonea *et al.* gives

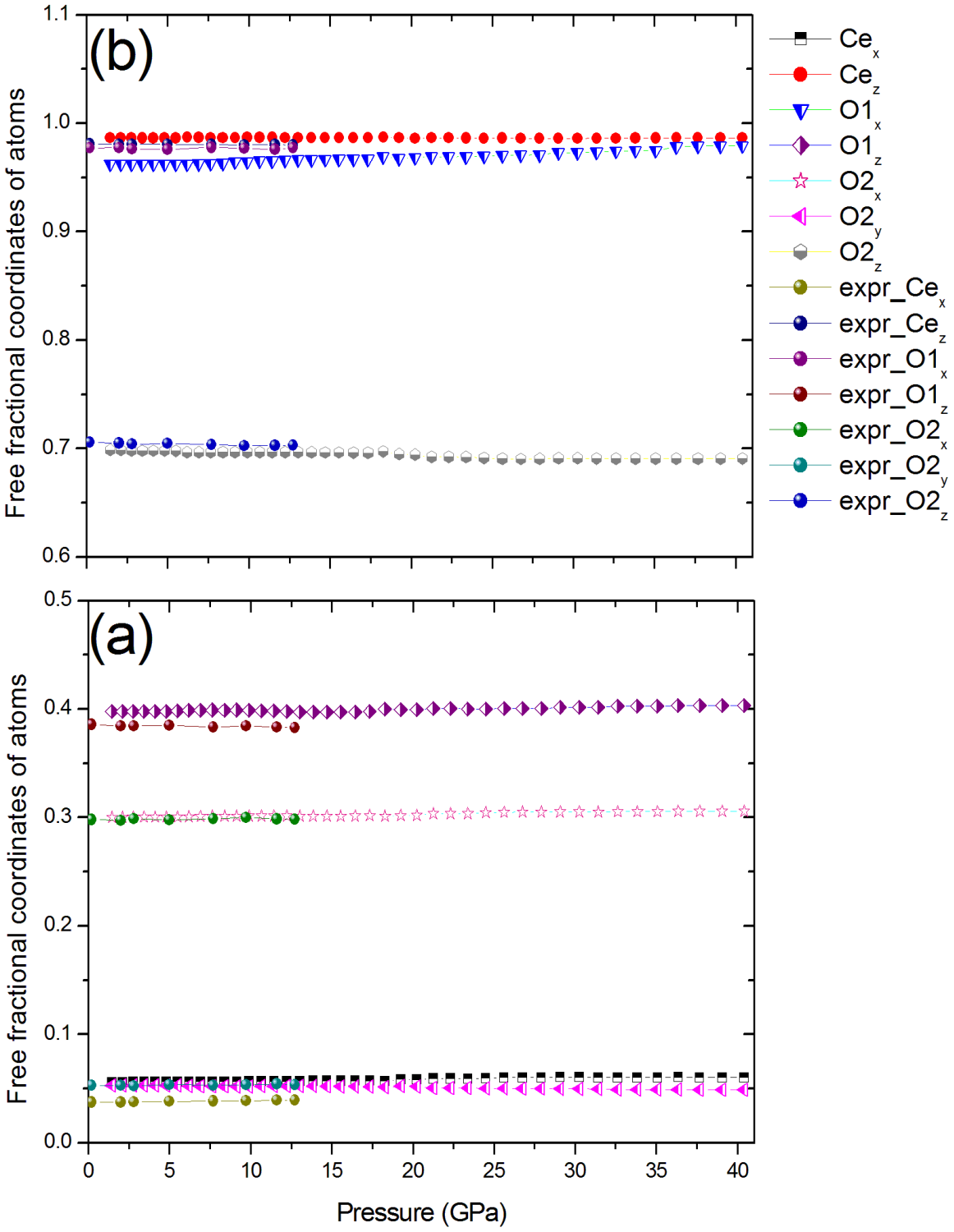

Figure 3: Pressure dependence of free fractional coordinates of atoms up to 40 GPa, compared to experiments from Ref.[10]

a value of 1.70×10^{-3} GPa^{-1}, we find $\kappa_c = 1.75 \times 10^{-3}$. A third order Birch–Murnaghan equation of state have been used to describe the pressure dependence of the unit-cell volume, providing the equilibrium volume (V_0), bulk modulus (B_0), and its first pressure derivative (B_0'), all evaluated at zero pressure and summarized in Table 1. Ultimately, it is shown that the use of the GGA-PBEsol+U approximation gives a good agreement with respect to the available experimental data of Refs. 10 and 38. The calculated bulk modulus is very close to the measured one and confirms the low compressibility of the $CeScO_3$ compound.

For a complete assessment of our analysis, we gather in Table 2 our relaxed atomic positions. It is shown that the comparison with the experiments at ambient pressure is quite good. In order to check the influence of pressure on the polyhedral units of the $CeScO_3$, we also give the evolution of the internal positions as a function of pressure, see Fig. 3. As can be noted, the evolution of free atomic positions is very close to the experimental data in the pressure range where the comparison is possible. Consequently, we expect that calculations will properly describe the pressure dependence of bond lengths between atoms and polyhedral volumes in the pressure range of the present study.

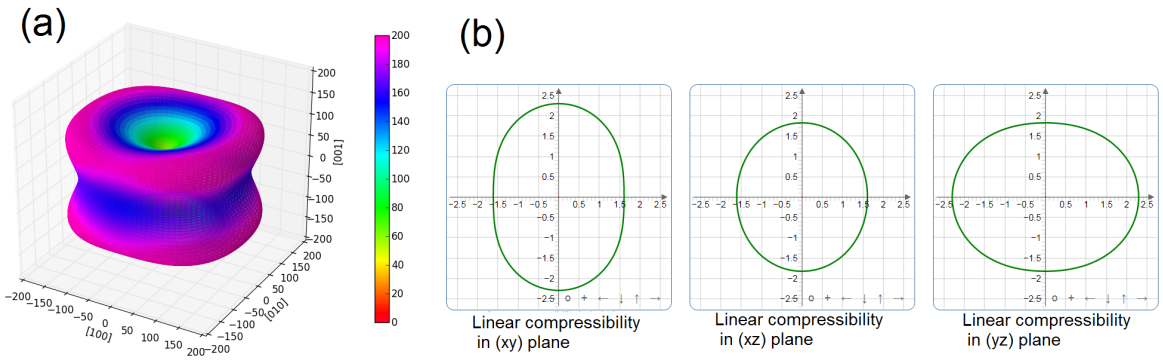

Figure 4: (a) 3D representation of the Young modulus (in GPa). (b) 2D map of the linear compressibility (in 10^{-3} GPa^{-1})

Table 3: Calculated effective elastic constants $\overline{C}_{ij}$ and elastic moduli at different pressures in GPa units.

P	$\overline{C}_{11}$	$\overline{C}_{22}$	$\overline{C}_{33}$	$\overline{C}_{44}$	$\overline{C}_{55}$	$\overline{C}_{66}$	$\overline{C}_{12}$	$\overline{C}_{13}$	$\overline{C}_{23}$
0	290.713	261.023	282.302	72.737	79.120	75.603	120.603	139.728	113.232
10	316.238	306.774	296.078	69.188	78.982	72.436	162.359	190.171	181.326
20	332.319	347.212	315.059	65.177	77.392	70.560	200.307	242.652	199.145
30	346.638	389.258	309.601	57.404	71.134	65.153	245.237	278.550	242.111
40	353.155	392.964	312.751	49.658	64.795	59.429	275.719	321.985	277.672
	B_V	B_R	B_H	Y_V	Y_R	Y_H	G_V	G_R	G_H
0	175.68	174.5	175.09	199.67	199.01	199.34	76.177	75.96	76.069
10	220.76	220.59	220.67	189.44	186.38	187.91	69.803	68.563	69.183
20	253.2	252.8	253	182.49	172.84	177.67	66.125	62.349	64.237
30	286.37	283.98	285.17	161.36	138.09	149.77	57.378	48.658	53.018
40	312.18	302.49	307.33	134.29	50.676	93.091	47.009	17.213	32.111

Table 4: Calculated eigenvalues of the stiffness matrix in GPa units

P	λ_1	λ_2	λ_3	λ_4	λ_5	λ_6
0	72.737	75.603	79.055	146.28	159.19	528.57
10	69.188	72.436	78.982	107.52	149.17	662.4
20	65.177	70.56	77.392	80.711	154.06	759.82
30	48.293	57.404	65.153	71.134	137.57	859.64
40	9.0724	49.658	59.429	64.795	112.94	936.86

ELASTIC CONSTANTS CALCULATIONS

In order to assess the stability of $CeScO_3$ and further understand its anisotropic structural behavior under hydrostatic pressure, we have calculated the elastic properties of this compound. In particular, the effective elastic constants $\overline{C}_{ij}$ have been determined. The effective elastic constants of orthorhombic $CeScO_3$ under pressure are defined in terms of the elastic constants at zero pressure (C_{ij}) as[48] :

$$\overline{C}_{\alpha\alpha} = C_{\alpha\alpha} - P;\ \overline{C}_{\alpha\beta} = C_{\alpha\beta} + P \quad (\alpha = 1, 2 \cdots, 6; \beta = 1, 2 \cdots, 6).$$

For orthorhombic crystals, the mechanical stability condition requires that the effective elastic constants satisfy the following stability criteria:[48]

$$\overline{C}_{11} > 0,\ \overline{C}_{44} > 0;\ \overline{C}_{55} > 0,\ \overline{C}_{66} > 0; \tag{1}$$

$$\overline{C}_{11}\overline{C}_{12} > \overline{C}_{22}^2; \tag{2}$$

$$\overline{C}_{11}\overline{C}_{22}\overline{C}_{33} + 2\overline{C}_{12}\overline{C}_{13}\overline{C}_{23} - \overline{C}_{11}\overline{C}_{23}^2 - \overline{C}_{22}\overline{C}_{13}^2 - \overline{C}_{33}\overline{C}_{12}^2 > 0; \tag{3}$$

The calculated effective elastic constants are collected in Table 3. There, it can be seen that the stability criteria of equations 1 to 3 are satisfied at pressures ranging from 0 to 40 GPa,[39–42] showing the mechanical stability of the orthorhombic phase of $CeScO_3$ in this pressure range. This is also confirmed by the fact that the stiffness matrix is positive definite at all pressures, as can be seen in the eigenvalues reported in Table 4. In addition, as can be seen from Table 3, only the elastic constants associated with shear deformations slightly decrease monotonically with pressure. Therefore, whereas the resistance of $CeScO_3$ to linear deformation is enhanced under HP, it is expected to slightly decrease as shear deformations are concerned.

For the sake of completeness, averaged macroscopic elastic moduli can be obtained from the C_{ij} components, like, bulk modulus (B), Young's modulus (Y), and shear modulus (G). All of them estimated at Voigt (V)[43] (uniform strain assumption), Reuss (R)[44] (uniform stress), and Hill (H)[45] approximations. The latter, being used for homogenized polycrystalline samples (see Table 3). It is found that B_R is comparable to the zero pressure bulk modulus parameter calculated from the EOS, which confirms the consistency of our elastic calculations. In order to examine the eventual anisotropy of the title compound, we have also studied the directional dependence[46] of the Young's modulus. The three-dimensional representation of Y is displayed in Fig. 4 (a). We have clear evidence that the Young modulus has not a spherical form, the surfaces indicate a drastic change in its shape. The directional dependency surface of Young modulus is deformed. Y_{max}= 212.11 GPa and Y_{min} = 188.58 GPa give an anisotropy ratio of 1.12. Additionally, to better understand the response of $CeScO_3$ to anisotropic stress, the linear compressibility[46] is also plotted, see Fig. 4(b). According to this plot, the compressibility is not isotropic for both **xy** and **yz** planes, confirming the analysis done before on the response of lattice parameters to pressure. On the other hand. in the **xz** plane anisotropy is reduced. In particular, from the elastic constant calculations we got $\kappa_a = 2.0 \times 10^{-3}$ GPa^{-1}, $\kappa_b = 2.5 \times 10^{-3}$ GPa^{-1}, and $\kappa_c = 1.8 \times 10^{-3}$ GPa^{-1}. Each value differs by less than 10 % of the values obtained from Fig. 2. The sequence of compressibilities is the same $\kappa_b > \kappa_a > \kappa_c$, but the anisotropy is slightly smaller in the **xz** plane according to elastic constants calculations. This is related to the fact that the difference between $\overline{C}_{33}$ and $\overline{C}_{11}$, the resistances to tensile or compressive deformations along the **z**- and **x**-directions, is nearly 5 %.

In Table 3 it can be seen that $\overline{C}_{55} > \overline{C}_{66} > \overline{C}_{44}$ which indicates that the [001](100) shear is easier than the [010](001) shear, which in turn is also easier than the [100](010) shear. Also, $\overline{C}_{11}$, $\overline{C}_{22}$, and $\overline{C}_{33}$ are considerably larger than $\overline{C}_{66}$, $\overline{C}_{55}$, and $\overline{C}_{44}$ which indicates that $CeScO_3$ has a greater resistance to unidirectional compression than to shear deformation. This can be seen also by comparing the bulk and shear moduli in Table 3. This difference

on directional compression is enhanced under compression as can be seen in Table 3; $\overline{C}_{11}$, $\overline{C}_{22}$, and $\overline{C}_{33}$ increase under pressure but $\overline{C}_{66}$, $\overline{C}_{55}$, and $\overline{C}_{44}$ decrease under pressure. This suggest that beyond 40 GPa there is tendency to favor a distortion of the crystal structure of $CeScO_3$; thus it can be speculated the transition at higher pressure to a lower symmetry phase. Finally, by using the correlation between the shear modulus and the Vickers hardness proposed by Teter,[47] we have estimated the hardness of $CeScO_3$ to be 11±2 GPa, which is similar to the hardness of quartz.

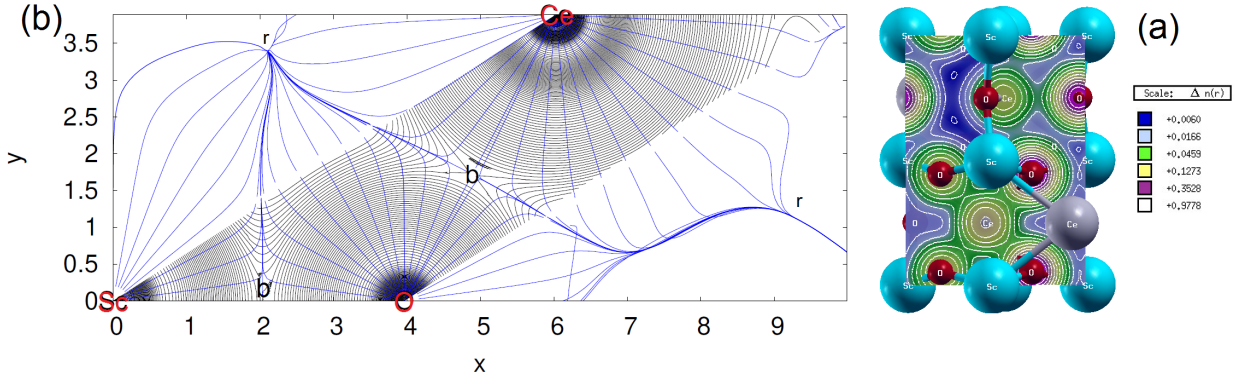

Figure 5: (a) Charge density (ρ) plot of the $CeScO_3$ in its denser plane, (b) Topological partition of ρ along the Sc-O-Ce bond. The black trajectories in (b) show the charge density (in electron/bohr^3). The set of trajectories colored in blue, represent the surface basins of Ce, Sc, and O respectively. The gradient path is defined from the condition of zero-flux surfaces $\boldsymbol{\nabla}\rho(\boldsymbol{r}) \cdot \boldsymbol{n}(\boldsymbol{r}) = 0$.

LOCAL COMPRESSIBILITY AND BONDING PROPERTIES

To further disclose and understand the compression mechanism of the orthorhombic $CeScO_3$ compound, we have also calculated the partition of the electronic density of the unit cell in terms of atomic contributions using the QTAIM strategy. This method provides a practical approximation to determine the compression mechanism at an atomic level. In this method, the electronic domain is divided into volumes labeled basins (Ω) that are disjoint, additives, and recover the unit cell volume.[18] In each of these basins, a number of critical points labeled (CP) emerge from the condition of zero flux of the gradient of the electron density:

$\boldsymbol{\nabla}\rho(\boldsymbol{r}) \cdot \boldsymbol{n}(\boldsymbol{r}) = 0$,[18] see Fig. 5. The integration of atomic properties inside the basins (Ω) gives us information about the chemical bonding of our compound, for example, the electron population N_Ω and the atomic volume V_Ω. From this calculation, we evaluate how the atomic compressibilities contribute to the bulk compressibility. To do this, we use the fact that the unit-cell volume can be expressed as :$V = \sum_\Omega V_\Omega$, and, then, we have calculated the compressibility as in Refs. 37, 49, and 50 using the following expressions:

$$\kappa = -\frac{1}{V}\sum_{\Omega}\left(\frac{\partial V_\Omega}{\partial p}\right)_T, \quad \kappa = \sum_{\Omega} f_\Omega \kappa_\Omega, \tag{4}$$

with

$$\kappa_\Omega = -\frac{1}{V_\Omega}\left(\frac{\partial V_\Omega}{\partial p}\right)_T, \quad f_\Omega = \frac{V_\Omega}{V}. \tag{5}$$

Table 5: QTAIM and polyhedral partition of the zero pressure bulk modulus and compressibility in terms of local bulk moduli (B_Ω(GPa)) and local compressibilities (κ_Ω(TPa^{-1})). f_Ω stands for the corresponding occupation factor. Only the fraction of the cubooctahedra inside the unit cell is considered (see text).

Ω	f_Ω	B_Ω(GPa)	κ_Ω(TPa^{-1})
Ce	0.272	220.8	4.5
Sc	0.128	211.2	4.7
O1	0.199	143.9	6.9
O2	0.401	154.9	6.5
CeO_{12}	0.805	172.4	5.8
ScO_6	0.195	158.4	6.3
unit-cell	1.000	171.9	5.8

The results are gathered in Table 5. The QTAIM partition depicts the oxygen ions as the more sensitive to the variation of pressure. However, two distinct compressibilities are shown for this atom. The O1 ion, which occupies the equatorial corners of ScO_6 polyhedra, is the most compressible one. The fractional occupation of the oxygen atoms, f_O, represents 60% of the unit cell. We can thus conclude that these anions mainly control the anisotropic compressibility of $CeScO_3$.

By calculating the ratio between the integrated charge inside each topological basin

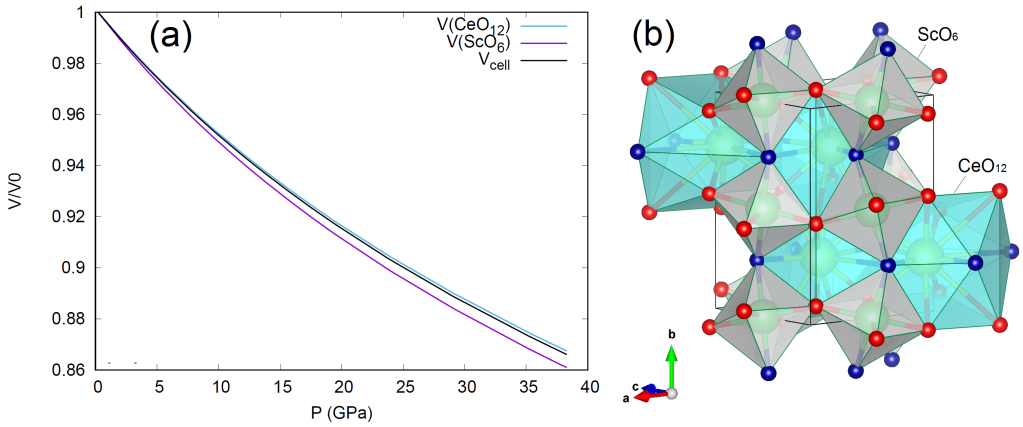

Figure 6: (a) Pressure dependence of the relative volume (V_0/V) of CeO_{12} cuboctahedra (blue line), ScO_6 octahedra (purple line) and unit cell volume (black line). (b) Polyhedral view of the $CeScO_3$ structure. CeO_{12} cuboctahedron and ScO_6 octahedra are represented as blue light and gray surfaces, respectively. Notice how two CeO_{12} units situated in the edges of the unit cell are defined with oxygen atoms of the adjacent unit cells.

and the corresponding oxidation number, we have evaluated the evolution of the degree of ionicity[52] as a function of pressure. It is seen that the ionicity decreases by ∼2% up to 40 GPa (from 73.3% to 71.8%). This weak change of chemical bonding might affect also other electronic properties as the band-gap,[53] see below. The distortion is however not very pronounced, which makes any structural transition hard to occur.

The polyhedral distortion was already analyzed in the benchmark work of Ref. 10 in terms of bond and Robinson parameters.[54] The study confirms that one of the Sc–O2 bonds is more affected by pressure than the other ones, but, only a weak difference was noticed. Albeit, due to the inequality of the local compressibility of the Ce and Sc cations, the distortion between ScO_6 and CeO_{12} units should be distinct. To evaluate the different compressibility of the polyhedra, we have fitted our calculated pressure-volume data for the ScO_6 and CeO_{12} units to a third-order Birch Murnaghan equation of state (see Fig. 6(a)). Local bulk modulus values of 158.36 GPa and 172.44 GPa for the ScO_6 and CeO_{12} polyhedra, respectively, are obtained. Interestingly, the volume defined by this polyhedral partition add up to a value greater than the unit cell volume when considering the number of formula units. This fact prevents an *a priori* partition of the bulk modulus of the $CeScO_3$ crystal

into local polyhedral compressibilities. However, it should be emphasized that two CeO_{12} cubo-octahedra are totally included within the unit cell whereas the other two, due to the high distortion of the CeO_{12} units, are defined involving O atoms of adjacent cells (see Fig. 6(b)). As a result, the occupation of these two cubo-octahedra in the unit cell is not equal to 2. We have checked that the calculated percentage of excess volume of these two cubo-octahedra shows a constant value regardless of the pressure (91.1% of the volume of these two CeO_{12} units is always inside the unit cell). This fact allows us to carry out a polyhedral partition following equivalent equations as those used for the atomic partition.

Since CeO_{12} cubo-octahedra share rhombic faces, while their triangular faces are common to those of the ScO_6 octahedra, the unit-cell volume is completely occupied by these two types of polyhedra. Therefore, we can express the unit cell volume as $4\times V(ScO_6) + 3.822\times V(CeO_{12})$. With this volume partition, we can now recover the bulk compressibility in terms of local polyhedral compressibilities. Using eq. (5) with the zero pressure calculated fractional volume occupations of 0.195 and 0.805 for ScO_6 and CeO_{12} units respectively, we obtain a bulk modulus of 169.52 GPa for the $CeScO_3$ crystal, in excellent agreement with the experimental B_0 value reported by Errandonea et al of 165 GPa. As it can be seen in Fig. 6(a), the local bulk modulus of the CeO_{12} cubo-octahedron is very close to the one of the unit cell, which is consistent with the polyhedral compressibility model developed for ox-ospinels by Recio *et al.*[55] Indeed, as the ratio $B(CeO_{12})/B(ScO_6)$ is almost equal to unit, no structural transformation is expected. This statement was defended in reference 10 resorting to the small difference of ionic radius between Ce^{3+} and Sc^{3+}, and now is corroborated in terms of the local compressibility analysis. As we have discussed above (see again Table 5), the volumes of oxygen ions are the more affected by pressure, especially that of the O1 ones, and ScO_6 octahedra are more compressed compared to the CeO_{12} octahedra. This analysis thus bridges the anisotropy of the structure with the distortion of the polyhedra. In particular, the rigidity of both CeO_{12} cuboctahedra and ScO_6 octahedra favors the stability of the crystal structure, making $CeScO_3$ very adapted to accommodate stress without violating the

geometric rules of perovskite.

Table 6: Experimental (ω_{Exp}) and calculated (ω_{DFT}) Raman modes of $CeScO_3$ (in cm^{-1}). The relative difference between experimental and calculated frequencies is also given in R_ω, as well as the experimental and theoretical pressure coefficients, $\frac{d\omega}{dp}$ (in cm^{-1}/GPa), and Grüneisen parameters (γ).

Mode	ω_{DFT}	ω_{Exp}	R_ω	$d\omega_{DFT}$ /dP	$d\omega_{Exp}$/dP	γ_{DFT}	γ_{Exp}
A_g	87.4			0.31		0.57	
B_{2g}	106.5	150	0.29	0.83	1.47	1.24	1.62
B_{2g}	129.4	182	0.29	0.96	1.20	1.18	1.08
A_g	137.8	188	0.27	1.71	2.33	1.98	2.04
B_{3g}	140.4	216	0.35	0.78	1.07	0.89	0.81
B_{1g}	173.2	243	0.29	1.80	3.32	1.66	2.26
B_{1g}	343.4	285	-0.20	1.60	1.66	0.74	0.96
A_g	370.3	322	-0.15	2.74	1.99	1.18	1.02
B_{2g}	394.8	337	-0.17	1.60	2.70	0.65	1.32
A_g	402.8	357	-0.13	1.95	3.04	0.77	1.40
B_{1g}	449.1	386	-0.16	1.57	0.53	0.56	0.23
B_{2g}	470.1	422	-0.11	2.55	1.63	0.87	0.64
A_g	471.7	436	-0.08	3.86	2.84	1.31	1.08
B_{3g}	475.1	470	-0.01	2.18	1.93	0.73	0.68
B_{3g}	504.0	492	-0.02	4.67	6.22	1.48	2.09
B_{1g}	519.2			3.68		1.13	
A_g	562.9	535	-0.05	3.27	4.50	0.93	1.39
B_{2g}	602.5	588	-0.02	3.73	3.31	0.99	0.93
B_{3g}	607.1			3.58		0.94	
B_{1g}	623.7	620	-0.01	5.21	8.35	1.33	2.52
B_{2g}	638.3			3.66		0.92	
A_g	657.6	656	0.00	3.95	1.98	0.96	0.50
B_{2g}	679.3			3.55		0.83	
B_{3g}	717.0			4.16		0.93	

LATTICE VIBRATIONS

We have calculated the phonon dispersion of $CeScO_3$ and found that there are no imaginary frequencies in the pressure range of this study. This is consistent with the fact that the orthorhombic structure remains stable up to 40 GPa as found in experiments.[10] In Fig. 7, we show the calculated phonon dispersion at ambient pressure and at 40 GPa along with the projection of the density of vibrational states onto the atomic constituents of $CeScO_3$. At

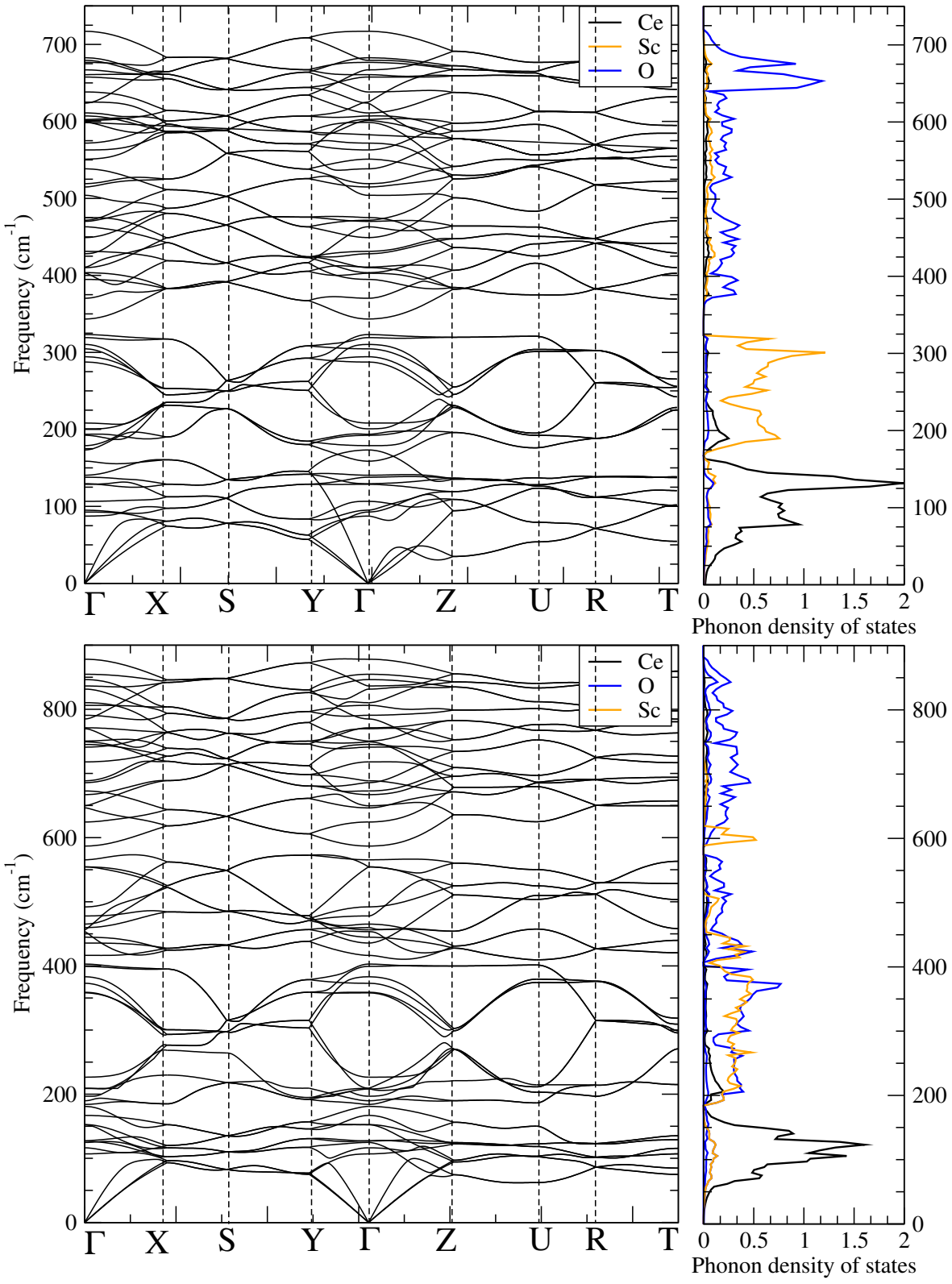

Figure 7: Phonon dispersion and phonon density of states of $CeScO_3$, top at zero pressure and bottom at 40 GPa. The partial DoS (PDoS) projected onto Ce, Sc, and O are also presented with black, orange and blue color, respectively.

the center of the Brillouin zone (Γ point), the factor group analysis provides the following decomposition corresponding of the sixty vibrations: $\Gamma_{acoustic} = B_{1u}+B_{2u}+B_{3u}$ and $\Gamma_{optical} = (7A_g + 5B_{1g} + 7B_{2g} + 5B_{3g})$ Raman-active + $(9B_{1u} + 7B_{2u} + 9B_{3u})$ IR-active + $8A_u$ silent modes. According to the phonon density of states (PDOS), the low-frequency motions are mainly due to Ce^{3+} ions (< 200 cm^{-1}), while the phonon modes with frequencies between 200 and 350 cm^{-1} have a major contribution of Sc^{3+}. Finally, higher frequencies belonging to high optical branches are predominant by oxygen anions. They can be described basically as internal vibrations of the ScO_6 octahedron, being by analogy with other scandates, the highest frequency modes associated to stretching vibrations of this octahedron.

To compare the results of calculations with experiments; we will first present the results of Raman measurements. Fig. 8 shows the pressure evolution of Raman spectra. The different modes shift towards higher frequencies under compression. A few modes merge because of their different pressure dependences. No evidence of phase transitions are found in Raman experiments up to 12.7 GPa in agreement with previous X-ray diffraction experiments.[10] In our measurements, we have identified 18 of the 24 Raman-active modes of $CeScO_3$. By means of a multi-Gaussian fit[56] we have determined the frequency of the modes at different pressures. The fit of the Raman spectrum measured at 0.8 GPa is shown in Fig. 9. The results are summarized in Fig. 9. Most modes show a linear behavior, with only a few of them show a non-linear pressure dependence of frequencies. For instance, the B_{1g} mode with 243 cm^{-1} frequency at 0.8 GPa.

With the help of DFT calculations, we have proposed a possible mode-assignment for Raman-active modes. Frequencies of calculated modes at zero pressure and measured modes at 0.8 GPa are represented by ticks in Fig. 8. In Table 6, we compare calculated and measured frequencies and propose a possible mode assignment; which should be validated by future polarized Raman experiments. We also report pressure coefficients and Grüneisen parameters. In order to do the mode assignment, we first correlate the frequencies of modes measured above 470 cm^{-1} with calculations. The differences in frequencies are smaller than

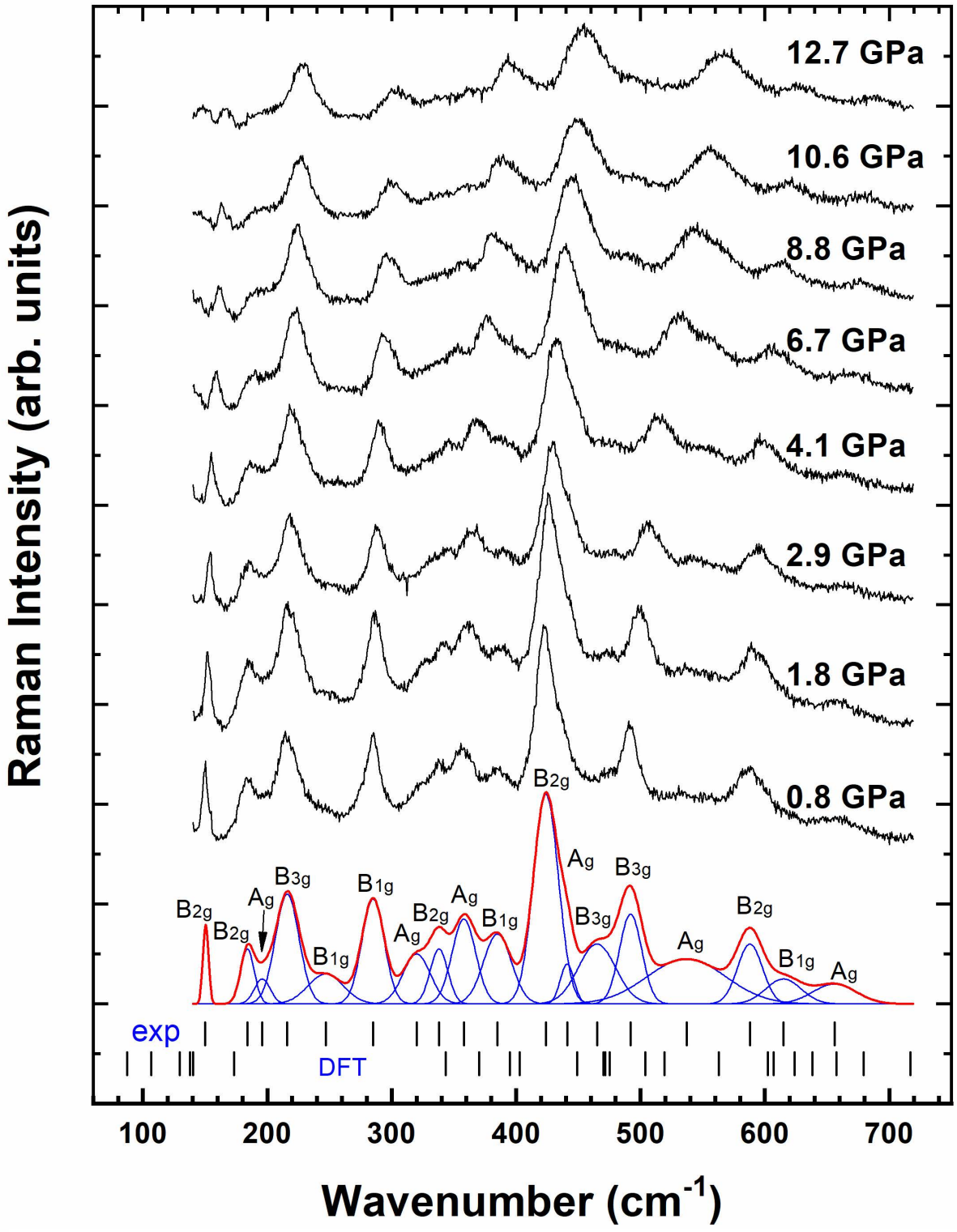

Figure 8: Raman spectra measured at different pressures indicated in the figure. At the bottom we show the multi-Gaussian fit to the lowest pressure spectrum (0.8 GPa).

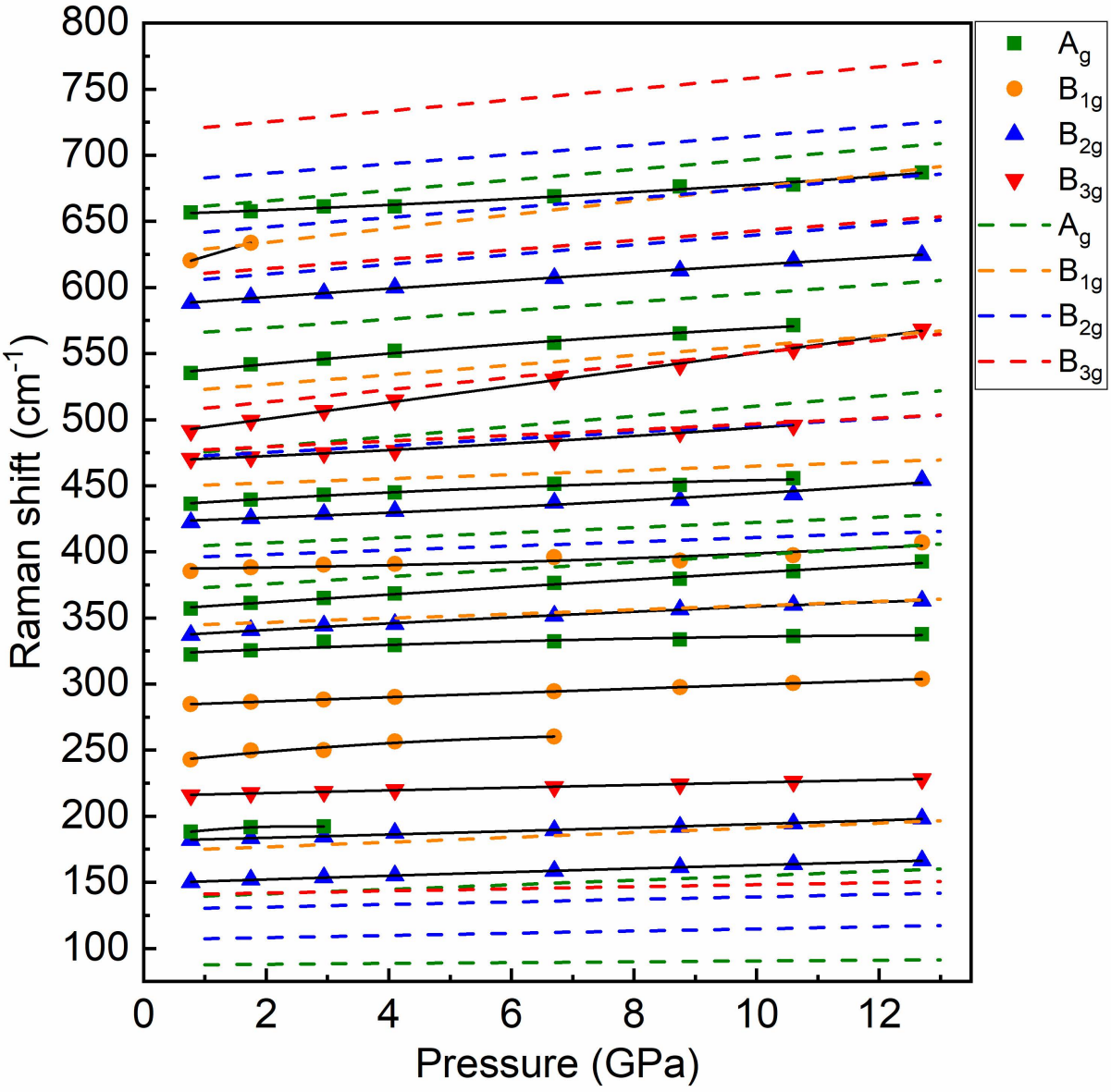

Figure 9: Pressure dependence of Raman modes obtained from experiments. Symbols are experimental results. Different symbols correspond to different type of modes (see figure for assignment). The lines are fits to experiments.

Table 7: Calculated IR modes of $CeScO_3$ (in cm^{-1}) and pressure coefficients (in cm^{-1}/GPa)

Mode	ω	$\frac{d\omega}{dp}$
B_{1u}	95.0	0.47
B_{3u}	128.7	0.40
B_{2u}	158.7	0.05
B_{1u}	178.9	0.39
B_{3u}	192.3	0.49
B_{2u}	208.2	0.50
B_{1u}	294.3	1.73
B_{2u}	304.6	1.83
B_{3u}	310.3	1.92
B_{3u}	319.2	2.13
B_{1u}	323.1	2.04
B_{2u}	410.1	1.41
B_{3u}	410.8	1.61
B_{3u}	428.1	1.98
B_{1u}	431.2	1.23
B_{1u}	463.1	2.57
B_{1u}	538.4	3.58
B_{2u}	551.0	3.72
B_{3u}	571.8	3.96
B_{2u}	598.7	3.91
B_{3u}	601.2	3.56
B_{1u}	611.0	3.87
B_{3u}	660.8	3.67
B_{2u}	676.7	4.63
B_{1u}	682.6	4.16

5%. This can be seen in the column that represents $R_\omega = (R_{\omega_{exp}} - R_{\omega_{DFT}})/R_{\omega_{exp}}$, which is the relative difference between frequencies. This agreement is excellent and as good as in other ternary oxides,[57,58] making the assignment of these modes plausible. At lower frequencies, there are 13 calculated modes and 12 measured modes. Since the calculated frequency of the lowest frequency mode is way below the cut-off frequency of our Raman set-up, we tentatively assign the 12 measured modes with the 12 calculated modes with frequencies higher than 100 cm^{-1}. We correlate these modes by ordering them by frequency. For the measured modes between 450 cm^{-1} and 320 cm^{-1} the agreement is still reasonable, with differences smaller than 17%. However, for the modes with measured frequencies smaller than 285 cm^{-1}, the agreement is poor, reaching the difference a maximum of 35% as can be seen in Table 6. Interestingly, the high-frequency modes are mostly related to internal vibrations of the ScO_6 octahedron, while the low-frequency modes involve mainly the movement of Ce atoms and ScO_6 octahedra as rigid units. The reason why DFT systematically underestimates the frequency of such modes could be related to the GGA/PBE exchange-correlation functionals used to describe Ce. The GGA/PBE has been shown to lead lattice under the binding which would result in phonon frequencies underestimations[58] as seen in this work. An important conclusion supported both by experiments and calculations is the non-existence of soft modes in $CeScO_3$, which is consistent with the extreme structural stability of this compound in comparison with other lanthanide perovskites.[59]

In addition to Raman modes, we have also calculated the pressure dependence of IR-active modes. There are no experimental results to be compared with. We include the results of IR modes for completeness and to facilitate the identification and assignment of IR modes in future experiments. The results are summarized in Table 7. There, it can be seen that IR covers a similar frequency range than Raman modes. The pressure coefficients are also similar to Raman modes, being the high-frequency phonons more sensitive to pressure than the low-frequency phonons. According to calculations, there are no IR modes (and not Raman modes) softening under compression.

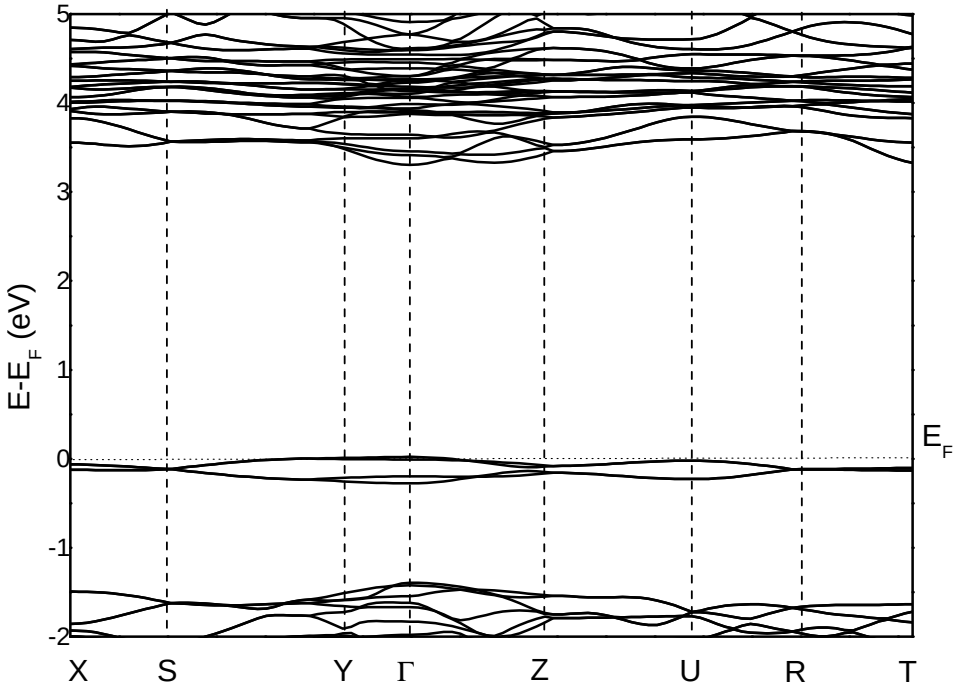

Figure 10: Band structure of the $CeScO_3$ compound calculated using PBEsol+U.

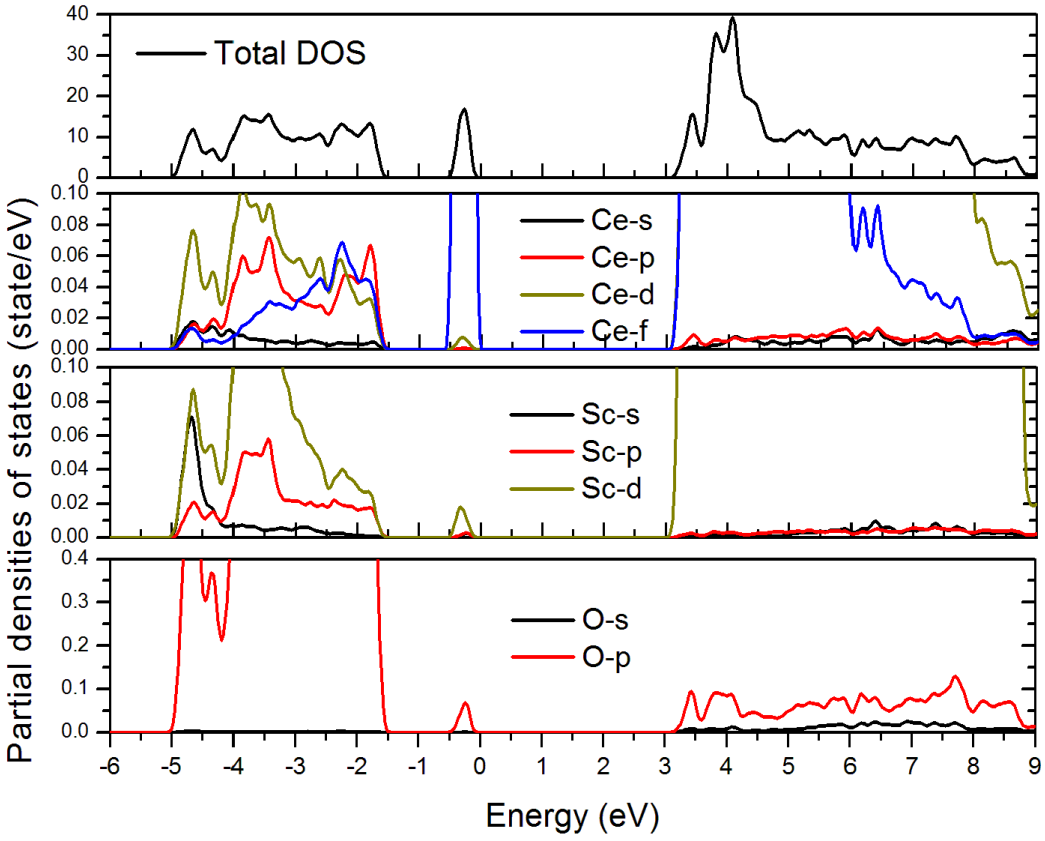

Figure 11: Calculated total and partial densities of states of the $CeScO_3$ compound using PBEsol+U.

ELECTRONIC PROPERTIES

When studying the band structure of $CeScO_3$ we found that VASP underestimates the band-gap as happens in other oxides.[60] In contrast, WIEN2K gives a more realistic value for the band-gap energy. Thus, the study of the electronic properties under HP has been done with WIEN2K. Due to the localized f-state of the Ce^{+3} cation on the Fermi level, we have used the Hubbard correction in order to predict the electronic properties.[28] In order to eliminate this localization, the on-site repulsion U was chosen equal to 4.57 eV. The as-obtained band structure plot within WIEN2K code is shown in Fig. 10. As observed in Fig. 10, the ambient structure of $CeScO_3$ presents a direct band-gap, whose valence band maximum (VBM) and conduction band minimum (CBM) are located at the Γ point. Our GGA-PBEsol+U calculation estimates a bandgap value of $E_g = 3.23$ eV, which is in good agreement with the value calculated by Shukla *et al*,[8] $E_g = 3.2$ eV. Regarding the topology of the band structure, we note that the conduction band is very dispersive, whereas, the valence band seems to be much less dispersive. This feature indicates that the title compound, which is known to be a p-type semiconductor,[8] will have a low-conductivity, due to the large effective mass of the holes in the valence band, a consequence of the flat characteristic of the valence band.[61]

To analyze the energetic contribution of each orbital of the investigated compound, we display in Fig. 11, the electronic partials density of states. An important feature related to the application of semi-local functional (U) is the shift of localized Ce-f orbitals. This one is accompanied by a strong hybridization with the O-p orbital near the Fermi level. Curiously this orbital is not found in the PDOS plot done with VASP code in Refs.[8] This fact is probably due to the discrepancy of VASP code to properly describes strongly correlated f and d-Ce states[30] and to the fact that they do not include this orbital in their pseudo-potential calculation. The near-upper valence bands between -6 to -2 eV are composed mostly of hybridized Sc-d, Ce-d, and O-p states and close to what was found in the work by Shukla *et al.*[8]

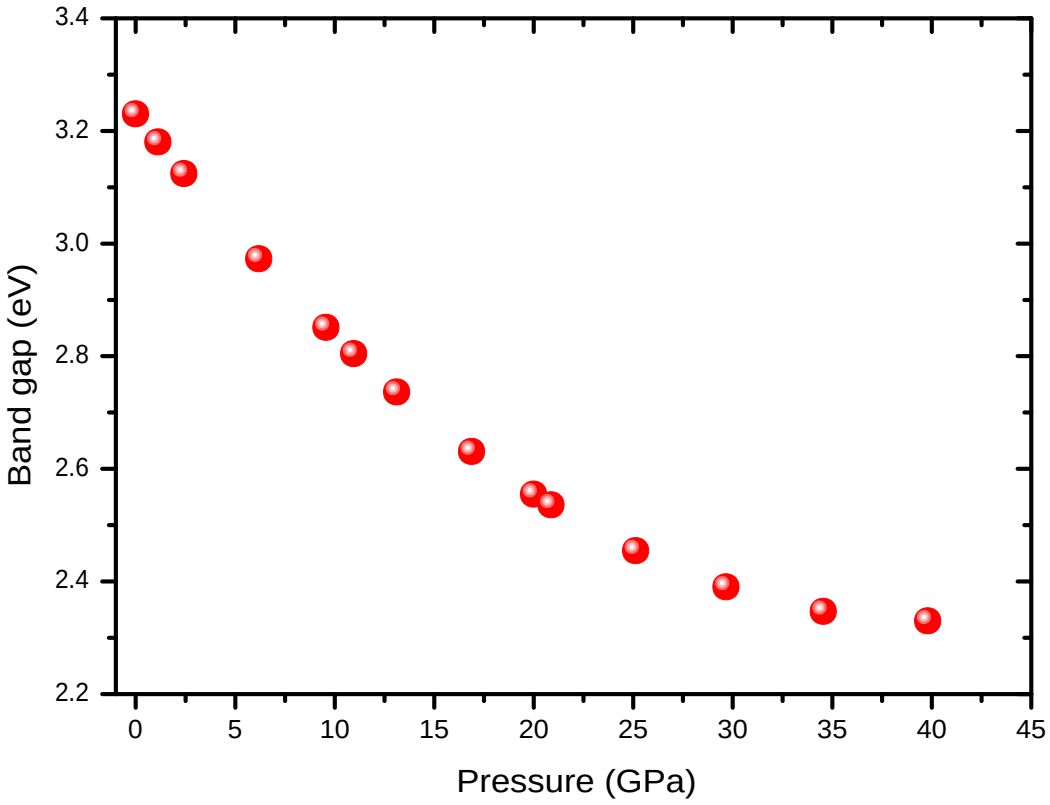

Figure 12: Calculated band gap evolution as a function of pressure.

To complete the picture of $CeScO_3$ under compression and probe the variations of the electronic properties as a function of pressure, we present in Fig. 12, the evolution of band-gap vs P. It is shown that the band-gap is clearly influenced by the increase in pressure. This fact is mainly due to the delocalization of the Ce-f electrons and an increase of O-p–Sc-d hybridization. A combination of this trend and the decrease of ionicity, implies a decrease of the electronic bandgap value. $CeScO_3$ has a considerably smaller band gap than other rare-earth scandates due to the contribution of Ce-f orbitals to the top of the valence band. This phenomenon has been observed previously in other ternary oxides; for instance, vanadates.[62] The fact that the Ce states are highly localized at ambient pressure makes the band gap to close under compression, as a consequence of a pressure-induced delocalization and increase of orbital hybridization.

CONCLUSIONS

We have found that density-functional theory within the semi-local functional GGA-PBEsol approximation, and including the Hubbard correction; describes accurately the high-pressure behavior of the crystal structure of $CeScO_3$. Such calculations provide also information on elastic constants, phonons, and electronic properties and their behavior under high-pressure conditions. From a microscopic point of view, we have also expressed the bulk compressibility in terms of a sum of atomic domain contributions in the sense of the atoms in molecules approach. The results show good agreement with the experiments. In addition, the average of the two polyhedral compressibilities (CeO_{12} and ScO_6) is found to recover the bulk value. The polyhedral units show a slight preference for the reduction of the cubo-octahedron as pressure is applied. The vibrational study has been completed with Raman experiments which have been reported for the first time including Raman-active phonon frequencies and their pressure dependence. All vibrational modes (Raman, infrared, and silent) have been assigned and related to atomic vibrations. Their pressure dependence has been also reported showing

that all modes harden under compression. Both, phonon and elastic-constant calculations are consistent with the structural stability of the orthorhombic perovskite-type structure of $CeScO_3$ up to 40 GPa. Finally, we provide a description of the electronic band structure, showing that $CeScO_3$ has a much smaller band-gap than other scandates due to Ce f-electrons. Such electrons also cause the closing of the electronic band-gap under compression. The band-gap energy is reduced by 30% in the pressure range covered by this study.

AUTHOR INFORMATION

Corresponding Author

* E-mail: daniel.errandonea@uv.es; tarik_ouahrani@yahoo.fr

ORCID

Daniel Errandonea: 0000-0003-0189-4221

Tarik Ouahrani: 0000-0002-1315-7870

Author Contributions

The manuscript was written through the contributions of all authors. All authors have given approval to the final version of the manuscript.

Notes

The authors declare no competing financial interest.

Acknowledgement

D.E. acknowledges the financial support given by the Spanish Ministry of Science, Innovation, and Universities (MCIU) under Grant Nos. PID2019-106383GB-C41 and RED2018-102612-T (MALTA Consolider-Team network) and by Generalitat Valenciana under Grant Prometeo/2018/123 (EFIMAT). R.F. and A. Lobato are grateful to financial support from

Spanish MCIU under Grant PGC2018-094814-B-C22. We would like to thank TGCC under the allocation 2020-A0080910433 made by GENCI, the PMMS (Pôle Messin de Modélisation et de Simulation), the Tirant supercomputer (Universitat de Valencia), and the MALTA-Consolider facilities for providing us the computational resources. SG and MB also acknowledge financial support through the COMETE project (Conception in silico de Matériaux pour l'Environnement et l'Energie) co-funded by the European Union under the program "FEDERFSE Lorraine et Massif des Vosges 2014-2020". The authors thank S. N. Achary for helpful discussions. A. L. and D. E. would like to thank the Generalitat Valenciana for the Ph.D. fellowship GRISOLIAP/2019/025).

References

(1) Asano, H.; Ogale, S. B.; Garrison, J.; Orozco, A.; . Li, Y. H; Li, E.; Smolyaninova, V. ; Galley, C.; Downes, M.; Rajeswari, M.; Ramesh, R. Venkatesan, T.; Pulsed-laser-deposited epitaxial Sr_2FeMoO_{6-y} thin films: Positive and negative magnetoresistance regimes. *Appl. Phys. Lett.* **1999**, *74*, 3696.

(2) Cohen, R.E. Origin of ferroelectricity in perovskite oxides. *Nature* **1992**, *358*, 136-138.

(3) Eom, C. B.; Cava, R. J.; Fleming, R. M.; Phillips, J. M.; vanDover, R. B.; Marshall, J. H., Hsu, J. W. P.; Krajewski, J. J.; Peck Jr., W. F. Single-Crystal epitaxial thin films of the isotropic metallic oxides $Sr_{1-x}Ca_xRuO_3$ ($0 \leq x \leq 1$). *Science* **1992**, *258*, 1766-1769.

(4) Bockris, J., Khan S. Electrocatalysis: on the frontier. *Electrochem. Soc* **1985**, *85*, 890.

(5) Pan, L.; Zhu, G. *Perovskite materials: synthesis, characterisation, properties, and applications, Books*, IntechOpen, **2016**, *3936* DOI: 10.5772/60469

(6) Kundu, A. K. *Magnetic perovskites: synthesis, structure and physical properties*, Library of Congress Control Springer India 2016

(7) Christen, H. M.; Jellison, G. E.; Ohkubo, I.; Huang, S.; Reeves, M. E.; Cicerrella, E.; Freeouf, J. L.; Jia, Y.; Schlom, D. G. Dielectric and optical properties of epitaxial rare-earth scandate films and their crystallization behavior. *Appl. Phys. Lett.* **2006**, *88*, 262906.

(8) Shukla, R.; Arya, A.; Tyagi, A. K. Interconversion of perovskite and fluorite structures in Ce-Sc-O system. *Inorg. Chem.* **2010**, *49*, 1152–1157.

(9) Greedan, J. E.; Seto, K. Preparation, cell constants, and some magnetic properties of $CeScO_3$. *Mater. Res. Bull.* **1981**, *16*, 1479–1485

(10) Errandonea, D.; Santamaria-Perez, D.; Martinez-García, D.; Gomis, O.; Shukla, R.; Nagabhusan Achary, S.; Tyagi, A. K.; Popescu, C. Pressure Impact on the Stability and Distortion of the Crystal Structure of $CeScO_3$. *Inorg. Chem.* **2017**, *56* (14) , 8363–8371.

(11) Irshad, K. A.; Srihari, V.; Sanjay Kumar, D.; Ananthasivan, K. Jena, H. High-pressure structural stability, equation of state, and thermal expansion behavior of cubic HfO_2, *J. Am. Ceram. Soc* **2020**, *103*, 5374–5381

(12) Kennedy, B. J.; Vogt, T.; Martin, C. D.; Parise, J. B.; Hriljac, J. A. Pressure-induced orthorhombic to rhombohedral phase transition in $LaGaO_3$. *J. Phys.: Condens. Matter* **2001**, *13*, L925–L930.

(13) Ross, N. L.; Zhao, J.; Burt, J. B.; Chaplin, T. D. Equations of state of $GdFeO_3$ and $GdAlO_3$ perovskites. *J. Phys.: Condens. Matter* **2004**, *16*, 5721–5730.

(14) Lin, C.; Zhang, Y.; Liu, J.; Li, X.; Li, Y.; Tang, L.; Xiong, L. Pressure-induced structural change in orthorhombic perovskite $GdMnO_3$. *J. Phys.: Condens. Matter* **2012**, *24*, 115402.

(15) Angel, R. J.; Zhao, J.; Ross, N. L.; Jakeways, C. V.; Redfern, S. A. T.; Berkowski, M. High-pressure structural evolution of a perovskite solid solution $(La_{1-x}Nd_x)GaO_3$. *J. Solid State Chem.* **2007**, *180*, 3408– 3424.

(16) Benmakhlouf, A.; Errandonea, D.; Bouchenafa, M.; Maabed, S.; Bouhemadou, A.; Bentabet, A. New pressure-induced polymorphic transitions of anhydrous magnesium sulfate. *Dalton Trans.* **2017**, *46*, 5058–5068

(17) López-Moreno, S.; Errandonea, D.; Rodríguez-Hernández, P.; Muñoz, A. Polymorphs of $CaSeO_4$ under pressure: A first-principles study of structural, electronic, and vibrational properties. *Chem.* **2015**, *54*, 4.

(18) Bader, R. F. W. *Atoms in molecules: A quantum theory*; Clarendon Press: Oxford, U. K., p 438, 1990.

(19) Klotz, S.; Chervin, J.-C.; Munsch, P.; Le Marchand, G. Hydrostatic limits of 11 pressure transmitting media, *J. Phys. D: Appl. Phys.* **2009**, *42*, 075413.

(20) Errandonea, D.; Meng, Y.; Somayazulu, M.; Häusermann, D. Pressure-induced $\alpha \longrightarrow \omega$ transition in titanium metal: A systematic study of the effects of uniaxial stress. *Physica B* **2005**, *355*, 116.

(21) Mao, H. K.; Xu, J.; Bell, P. M. Calibration of the ruby pressure gauge to 800 kbar under quasi-hydrostatic conditions *J. Geophys. Res.* **1986**, *91*, 4673–4676.

(22) Kresse, G.; Hafner, J.; Ab initio molecular dynamics for liquid metals, Phys. Rev. B **1993**, *47*, 558–561.

(23) Kresse, G.; Furthmüller, J.; Efficiency of ab-initio total energy calculations for metals and semiconductors using a plane-wave basis set, *Comput. Mat. Sci.* **1996**, *6*, 15-50.

(24) Blöchl, P.E.; Projector augmented-wave method, *Phys. Rev. B* **1994**, *50*, 17953–17979.

(25) Perdew, J.P.; Ruzsinszky, A.; Csonka, G.I.; Vydrov, O.A.; Scuseria, G.E.; Constantin, L.A.; Zhou, X.; Burke, K. Restoring the density-gradient expansion for exchange in solids and surfaces *Phys. Rev. Lett.*, **2008** *100*, 136406,

(26) Srour, J.; Badawi, M.; El Haj Hassan, F.; Postnikov, A. Comparative study of structural and electronic properties of GaSe and InSe polytypes *J. Chem. Phys* **2018**, *149*, 054106

(27) Heyd, J.; Peralta, J. E.; Scuseria, G. E.; Martin, R. L. Energy band gaps and lattice parameters evaluated with the heyd-scuseria-ernzerhof screened hybrid functional. *J. Chem. Phys.* **2005**, *123*, 174101.

(28) Dudarev, S. L.; Botton, G. A.; Savrasov, S. Y.; Humphreys, C. J.; Sutton, A. P. Electron-Energy-Loss Spectra and the Structural Stability of Nickel Oxide: An LSDA+U Study. *Phys. Rev. B* **1998**, *57*, 1505–1509.

(29) Jochym, P.T.; Module for calculating elastic tensor of crystals, software, https://github.com/jochym/Elastic/

(30) Philippe, F. W.; Kim, E. Assessing Hubbard-corrected AM05+U and PBEsol+U density functionals for strongly correlated oxides CeO_2 and Ce_2O_3. *Phys. Chem. Chem. Phys.* **2016**, *18*, 26816-26826.

(31) Blaha, P.; Schwarz, K.; Sorantin, P.; Trickey, S.K. Full-potential, linearized augmented plane wave programs for crystalline systems. *Comput. Phys. Commun*, **1990**, *59*, 399.

(32) Giannozzi, P.; de Gironcoli, S.; Pavone, P.; Baroni, S. Ab initio calculation of phonon dispersions in semiconductors *Phys. Rev. B* **1991**, *43*, 7231.

(33) Gonze, X.; Lee, C.; Dynamical matrices, Born effective charges, dielectric permittivity tensors, and interatomic force constants from density functional perturbation theory. *Phys. Rev. B* **1997**, *55*, 10355.

(34) Togo, A.; Tanaka, I. First principles phonon calculations in materials science. *Scr. Mater* **2015**, *108*, 1–5.

(35) Baroni, S.; de Gironcoli, S.; Dal Corso, A.; Gianozzi, P. Phonons and related crystal properties from density functional perturbation theory. *Rev. Mod. Phys.* **2001**, *73*, 515.

(36) Otero-de-la-Roza, A.; Johnson, E. R.; Luaña, V. CRITIC2: A program for real-space analysis of quantum chemical interactions in solids, *Comput. Phys. Commun.* **2014**, *185*, 1007–1018.

(37) Martín Pendás, A.; Costales, A.; Blanco, M. A.; Recio, J. M.; Luaña, V. Local compressibilities in crystals. *Phys. Rev. B* **2000**, *62*, 13970

(38) Greedan, J.E.; Seto, K. Preparation, cell constants, and some magnetic properties of $CeScO_3$, *Mater. Res. Bull.* **1981**, *16*, 1479–1485.

(39) Gerward, L.; Olsen, J. S.; Powder diffraction analysis of cerium dioxide at high pressure. P*owder Diffr.* **1993**, *8*,127–129.

(40) Gerward, L.; Olsen, J. S.; Petit, L.; Vaitheeswaran, G.; Kanchana, V.; Svane, A. Bulk modulus of CeO_2 and PrO_2-An experimental and theoretical study. *J Alloy Compd.* **2005**, *400*, 56–61.

(41) Gurel, T.; Eryigit, R. Ab initio pressure-dependent vibrational and dielectric properties of CeO_2. *Phys Rev B.* **2006**, *74*, 014302.

(42) Belarouci, S.; Ouahrani, T.; Benabdallah, N.; Morales-García, Á.; Franco, R. Quantum-mechanical simulations of pressure effects on $MgIn_2S_4$ polymorphs, *Phase Transit.* **2018**, *91*, 759–771.

(43) Voigt, W. *Lehrbuch der Kristallphysik*, Teubner, Leipzig, 1928.

(44) Reuss, A.; Angew. Z. Berechnung der Fließlgrenze von Mischkristallen auf Grund der Plastizitätsbedingung für Einkristalle. *Math. Mech.* **1929**, *9*, 49.

(45) Hill, R. The Elastic Behaviour of a Crystalline Aggregate. *Proc. Phys. Soc. Lond. A* **1952**, *65*, 349.

(46) Ouahrani, T.; Ciftci, Y. O.; Mebrouki, M. Dynamical and anisotropic behavior of the $MSiP_2$ (M= Be, Mg, Cd, Zn and Hg) compounds. *J. Alloys Compd* **2014** *610*, 372–381.

(47) Teter, D.M. Computational Alchemy: The Search for New Superhard Materials. *MRS Bull.* **1998**, *23*, 22.

(48) Mouhat, F.; Coudert, F. Necessary and sufficient elastic stability conditions in various crystal systems, *Phys. Rev. B* **2014**, *90*, 224104

(49) Ouahrani, T.; Franco, R.; Menéndez, J.M.; Marqués, M., Recio, J.M. Microscopic partition of pressure and elastic constants in CdTe polymorphs, *J. Alloys Compd* **2014**, *592*, 150–156.

(50) Recio, J. M.; Franco, R.; Pendás, A. M; Blanco, M. A.; Pueyo, L.; Pandey, R. Theoretical explanation of the uniform compressibility behavior observed in oxide spinels. *Phys. Rev. B* **2001**, *63*, 184101.

(51) Ouahrani, T.; Merad-Boudia, I.; Baltache, H.; Khenata, R.; Bentalha, Z. Effect of pressure on the global and local properties of cubic perovskite crystals. *Phys. Scr.* **2011**, *84*, 025704.

(52) Mori-Sánchez, P.; Martín Pendás, A.; Luaña, V. A classification of covalent, ionic, and metallic solids based on the electron density. *J. Am. Chem. Soc.* **2002**, *124*, 14721.

(53) Boukri, K.; Ouahrani, T.; Badawi, M.; Demmouche, K.; Franco, R.; Recio, J. M. Disclosing the behavior under hydrostatic pressure of rhombohedral $MgIn_2Se_4$ by means of first-principles calculations. *Phys. Chem. Chem. Phys.* **2020**, *22*, 21909–21918.

(54) Robinson, K.; Gibbs, G. V.; Ribbe, P. H. Quadratic elongation: A quantitative measuer of distortion in coordination polyhedra. *Science* **1971**, *172*, 567–570.

(55) Recio, J. M.; Franco, R.; Martin Pendas, A.; Blanco, M. A.; Pueyo, L.; Pandey, R. Theoretical explanation of the uniform compressibility behavior observed in oxide spinels. P*hys. Rev. B: Condens. Matter Mater. Phys.* **2001**, *63*, 184101.

(56) Errandonea, D.; Gracía, L.; Lacomba-Perales, R.; Polian, A.; Chervin, J. C. Compression of scheelite-type $SrMoO_4$ under quasi-hydrostatic conditions: Redefining the high-pressure structural sequence. *J. Appl. Phys.* **2013**, *113*, 123510.

(57) Errandonea, D.; Muñoz, A.; Rodríguez-Hernández, P.; Gomis, O.; Nagabhusan Achary, S.; Popescu, C.; Patwe, S. J.; Tyagi, A. K. High-Pressure Crystal Structure, Lattice Vibrations, and Band Structure of $BiSbO_4$. *Inorg. Chem.* **2016**, *55*, 4958–4969.

(58) Liang, Q., Dwaraknath, S. Persson, K.A. High-throughput computation and evaluation of raman spectra. *Sci Data* **2019**, *6*, 135.

(59) Liu, C.-M.; Ge, N.-N.; Cheng, Y.; Ji, G.-F. Structural and elastic properties of $LaTiO_3$ under pressure. *Physica B: Condensed Matter* **2011**, *406*, 1926-1931.

(60) Panchal, V.; Errandonea, D.; Segura, A.; Rodriguez-Hernandez, P.; Muñoz, A.; Lopez-Moreno, S.; Bettinelli, M. The electronic structure of zircon-type orthovanadates: Effects of high-pressure and cation substitution. *Journal of Applied Physics* **2011**, *105*, 043723.

(61) Bernholc, J. and Pantelides, Sokrates T. Theory of binding energies of acceptors in semiconductors. *Phys. Rev. B* **1977**, *15*, 4935-4947.

(62) Errandonea, D. High pressure crystal structures of orthovanadates and their properties. *J. Appl. Phys.* **2020**, *128*, 040903.

TOC Graphic